SUPPLEMENTARY INFORMATION

Liquid Crystal Metasurface Enabled Hyperspectral Single-pixel Imaging

Jiewen Nie[1,2,3], Tao Chen[1], Shan Jiang[2], Peng Dai[2], Mike Pivnenko[2], Weijie Wu[2], Pengyao Niu[1,4], Sen Wang[1,4], Jirong Bao[1,4], Daping Chu[2,3*], Haining Yang[1]**

[1] School of Electronic and Science and Engineering, Southeast University, 2 Sipailou, Xuanwu District, Nanjing, Jiangsu, 210096, China

[2] Centre for Photonic Devices and Sensors, University of Cambridge, 9 JJ Thompson Avenue, Cambridge CB3 0FA, United Kingdom

[3] Cambridge University Nanjing Centre of Technology and Innovation, 23 Rongyue Road, Jiangbei New District, Nanjing, Jiangsu, 211500, China

[4] Chien-Shiung Wu College, Southeast University, 2 Southeast University Road, Jiangning District, Nanjing, Jiangsu, 211102, China

* *dpc31@cam.ac.uk*

** *h.yang@seu.edu.cn*

1. Analysis and Optimisation of Single-Pixel Imaging Setting

In this work, single-pixel imaging was implemented through a DMD amplitude-type spatial light modulator using the Hadamard basis. To reduce redundant information and optimise encoding efficiency, a "Russian doll" Hadamard basis ordering strategy[1] was adopted. The core idea was to sort the Hadamard basis from low to high spatial frequencies , which facilitated the natural selection of appropriate spatial frequency subsets for efficient encoding without the need for constant full-resolution sampling. The sampling ratio between the used sampling bases and the full-sampling Hadamard bases defines sampling efficiency.

To verify our analysis, we experimentally tested the relationship between imaging time and image quality under different sampling rates. The results are shown in Fig. S1a. The reconstruction error quantified the relative deviation of each reconstructed pattern from the reference pattern acquired at the maximum sampling ratio. Consequently, the reconstruction error under the maximum sampling ratio converged to zero. The green curve shows that sampling time increased almost linearly with higher sampling ratios. From the blue curve, we can see that when the sampling ratio reached 18.75%, the reconstruction error became relatively stable with no significant improvement. Figure S1b shows the reconstructed patterns at different sampling ratios, which visually match the error data. The target pattern was already clear enough to be easily distinguished as the sampling ratio reached 18.75%. This indicates that this sampling ratio is sufficient to collect the necessary information for the simple letter patterns used in our target. For a 64×64 resolution Hadamard basis, 18.75% sampling rate corresponds to 64×64×18.75% = 768 encoding patterns.

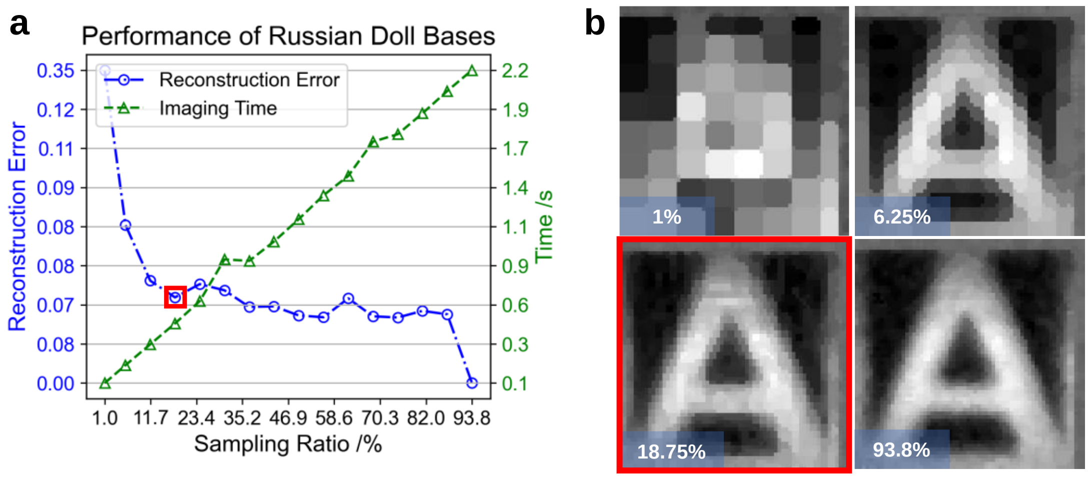

Figure S1. **a** Reconstruction error and sampling time as functions of sampling ratio under Matryoshka-style Hadamard basis ordering. **b** Reconstructed patterns at sampling ratios of 1%, 6.25%, 18.75%, and 93.8%.

2. Liquid Crystal Metasurface Simulation

The numerical modelling of liquid crystal (LC) metasurface was carried out by finite-difference time-domain (FDTD) simulations, with a particular emphasis on the background refractive index variations induced by the LC molecular orientation. Due to the surface anchoring effect, the rotational amplitude of LC molecules near the substrate interface was significantly constrained compared to those in the bulk region. This work employed an extended Oseen-Frank model[2,3] to calculate the non-uniform spatial distribution of the LC director under voltage-driven conditions. The equilibrium state of LC director $\boldsymbol{n}(z)$ was determined by minimising the total free energy functional:

$$F_{total} = \int \left[\frac{1}{2} K_{11} (\nabla \cdot \boldsymbol{n})^2 + \frac{1}{2} K_{22} (\boldsymbol{n} \cdot \nabla \times \boldsymbol{n})^2 + \frac{1}{2} K_{33} (\boldsymbol{n} \times \nabla \times \boldsymbol{n})^2 - \frac{1}{2} \epsilon_0 \Delta\epsilon (\boldsymbol{E} \cdot \boldsymbol{n})^2 \right] dz$$

where K_{11}, K_{22}, and K_{33} represent splay, twist, and bend elastic constants, respectively, $\Delta\epsilon$ denotes dielectric anisotropy, and **E** is the electric field. For a homogeneous alignment cell with a strong anchoring boundary condition ($\boldsymbol{n}_z(z = 0) = \boldsymbol{n}_z(z = d) = 0$), the threshold voltage V_0 is given by:

$$V_0 = \pi \sqrt{\frac{K_{11}}{\epsilon_0 |\Delta\epsilon|}}$$

Figure S2 illustrates the normalised thickness-dependent LC tilt angle distribution under various driving voltages. The thickness coordinate was normalised to [0,1], with boundary layers fixed at 0 rad due to strong anchoring. At low voltages, elastic deformation dominated, resulting in minimal variation in tilt angle. As voltage increased, dielectric coupling overcame elastic resistance, inducing progressive reorientation toward 0.5π in the central region. Notably, the non-uniform in-plane distribution of LC orientation requires further consideration for accurate optical response prediction.

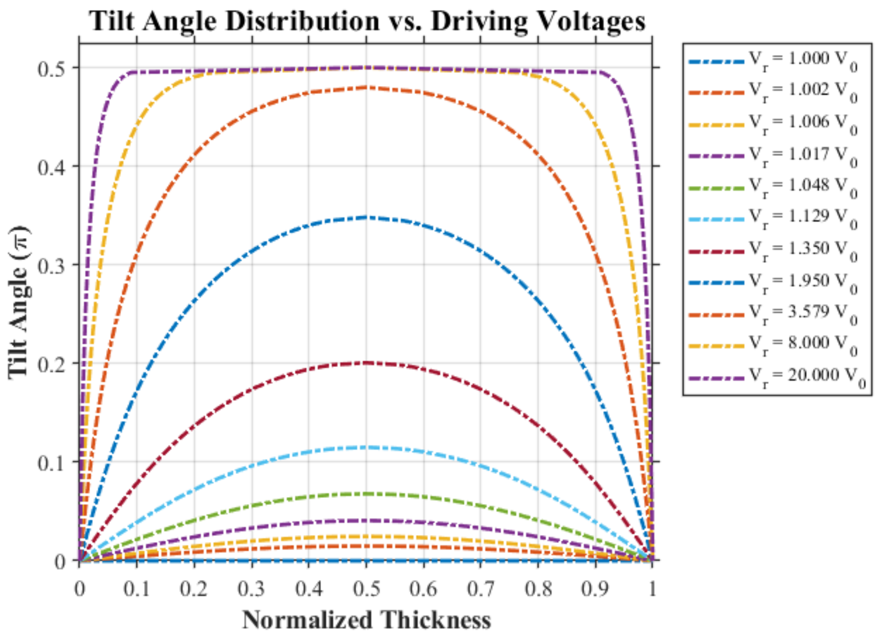

Figure S2. Voltage-controlled liquid crystal tilt angle distribution across normalised cell thickness.

A simplified simulation setup (Fig. S3) was implemented to evaluate displacement-induced alignment errors in bilayer metasurfaces. The displacement along the diagonal axis was systematically varied from 0 to $0.5*\sqrt{2}T$ (where T=800 represents the metasurface periodicity). Figure S4 presents the simulated zero-voltage transmission spectra for different displacement values. The spectral response variation was moderate and can be calibrated in such a broadband spectral encoding application.

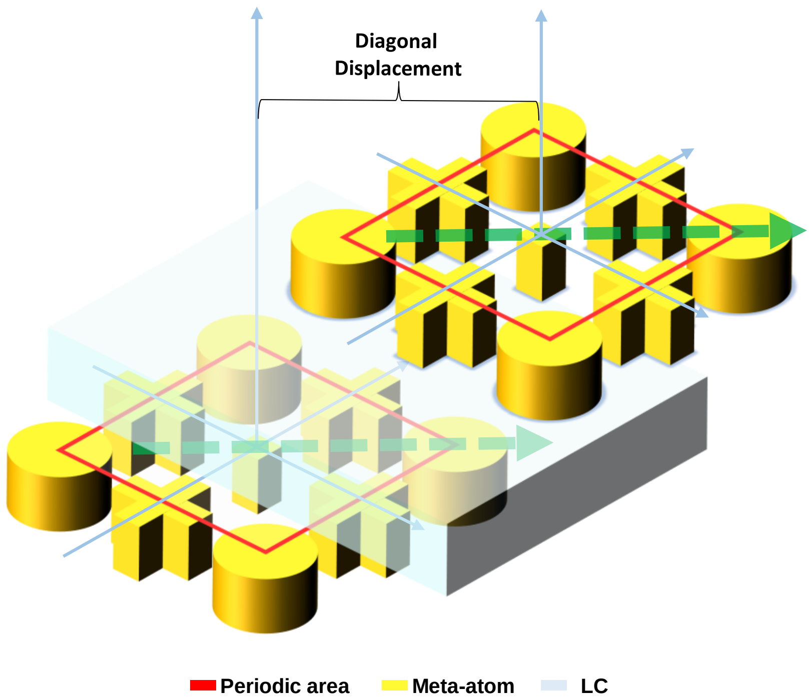

Figure S3. Structure of the LC-MS device with displacement along the diagonal axis (the green axis).

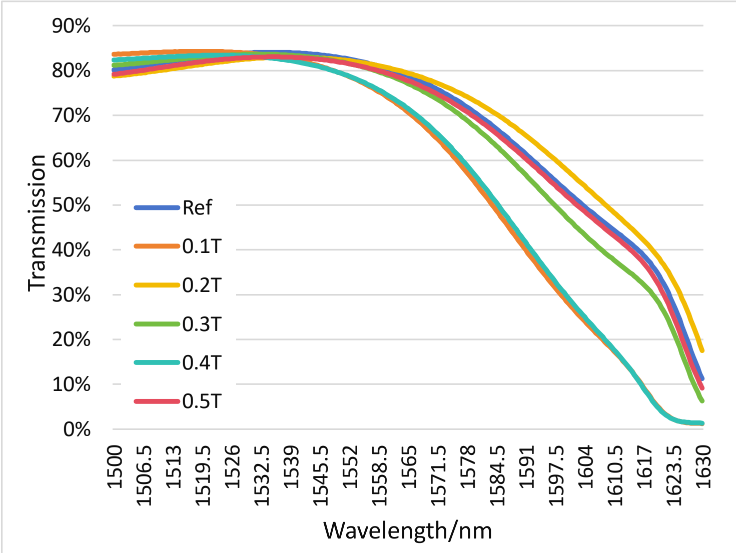

Figure S4. displacement sensitivity evaluation result of LC-MS. The simulated spectral transmission of LC-MS with different displacements.

3. Fabrication of Liquid Crystal Metasurfaces

Fabrication of the liquid crystal metasurfaces (Fig. S5) started with the ITO glass substrates. A photoresist layer was coated and patterned via electron beam lithography to define the metasurface geometries. Sequential thermal evaporation deposited a 10-nm chromium adhesion layer followed by a 100-nm gold layer, after which the lift-off processing in acetone revealed gold nanostructures. Photo-alignment material SD1 for the LC orientation was then spin-coated onto the metasurface-patterned substrates and directionally aligned using linearly polarised UV exposure. Two aligned substrates were assembled in an anti-parallel configuration using 4-μm spacers. The formed liquid crystal cell was subsequently vacuum-filled with high-birefringence nematic liquid crystal (Δn = 0.42).

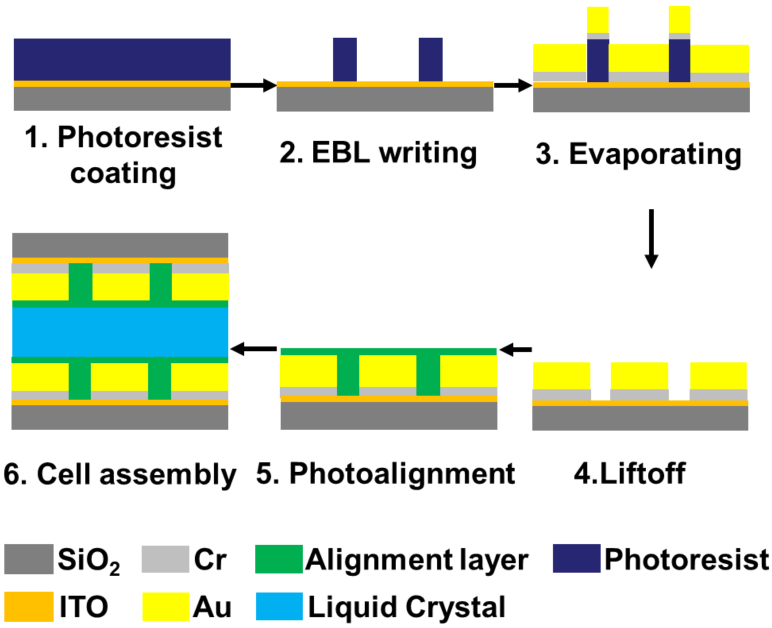

Figure S5. Process flow for liquid crystal metasurface (LC-MS) device fabrication.

4. Device Characterisation of Liquid Crystal Metasurfaces

Fig. S6 illustrates the optical setup used for spectral response calibration. A tunable laser (1500–1630 nm, 0.5 nm steps) illuminated a reference whiteboard to generate standardised excitation. The reflected light was detected through the single-pixel imaging system. By scanning the laser wavelength at constant optical power and recording corresponding detector outputs, we calibrated the full-system spectral response without characterising individual optical components or detector responsivity.

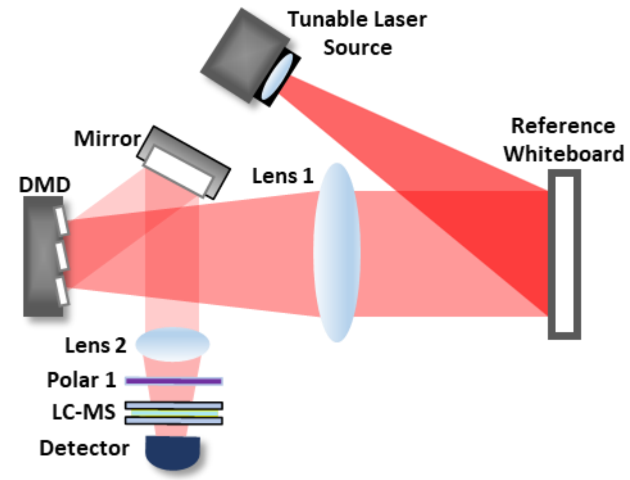

Figure S6. Spectral response calibration setup with reference source.

Fig. S7 depicts the inherent system spectral response (without LC-MS), representing the static baseline response measured without the tunable filter. This integrated characterisation accounts for the spectral transmission/response of the reference whiteboard, single-pixel imaging optics, and detector. Cumulative optical losses beyond 1550 nm cause significant responsivity degradation at longer wavelengths.

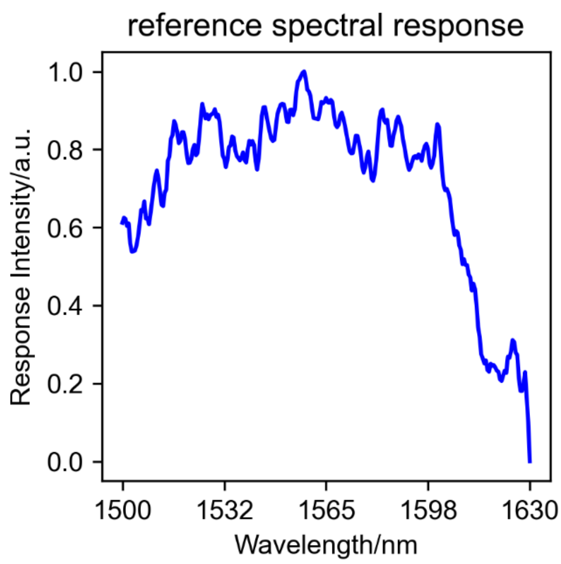

Figure S7. Inherent SPI system responsivity without LC-MS.

The response times of the LC-MS device were measured via the 10%–90% transition standard. Fig. S8 illustrates a representative step-response test, where the driving voltage (red) and corresponding optical response (blue) yield a transition time of ~2.5 ms. Note: Detected voltages diverged from applied values due to circuit loading.

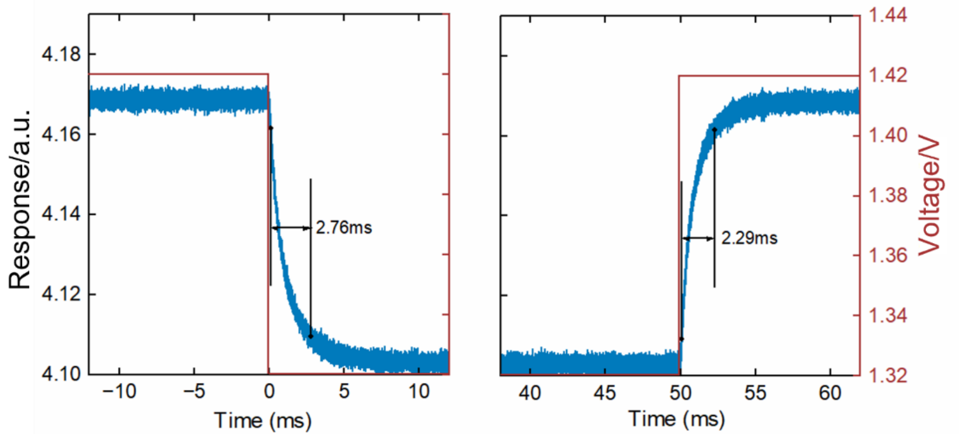

Figure S8. Step-response characterisation example (10%-90% transition).

5. Spectral Decoding via Conditional Generative Adversarial Network

The spectral reconstruction framework utilised a conditional generative adversarial network (C-GAN) architecture illustrated in Fig. S9. This adversarial system integrated a generator that reconstructed spectra from the encoded measurements, combined with randomly sampled latent vectors, alongside a discriminator that evaluated distributional consistency between predictions and ground-truth datasets. The detailed setting of the proposed c-GAN model is shown in Table S1. During training, each encoded measurement (condition signal) was coupled with multiple latent vectors to explore solution space diversity (The number of latent vectors was defined as Z_Number). This effectively mitigated the convergence challenges inherent to ill-posed inverse problems (i.e., one-to-many problems)[4]. The discriminator enforced statistical similarity through batch-level spectral distribution comparisons. [5]

For performance evaluation, this model was executed in a virtual environment (Python 3.9.18, PyTorch 2.1.0) with an Intel i5-13400 CPU and an NVIDIA GeForce RTX 4060 Ti GPU. The average reconstruction time per spectral signal was 0.38 ms. It should be noted that each signal to be decoded was repeated Z_Number times and then concatenated with Z_Number randomly sampled latent vectors. In this evaluation, Z_Number was set to 100, which meant that this reconstruction process undertook 100 forward inferences per spectrum. This indicates the process still has huge potential for speeding up.

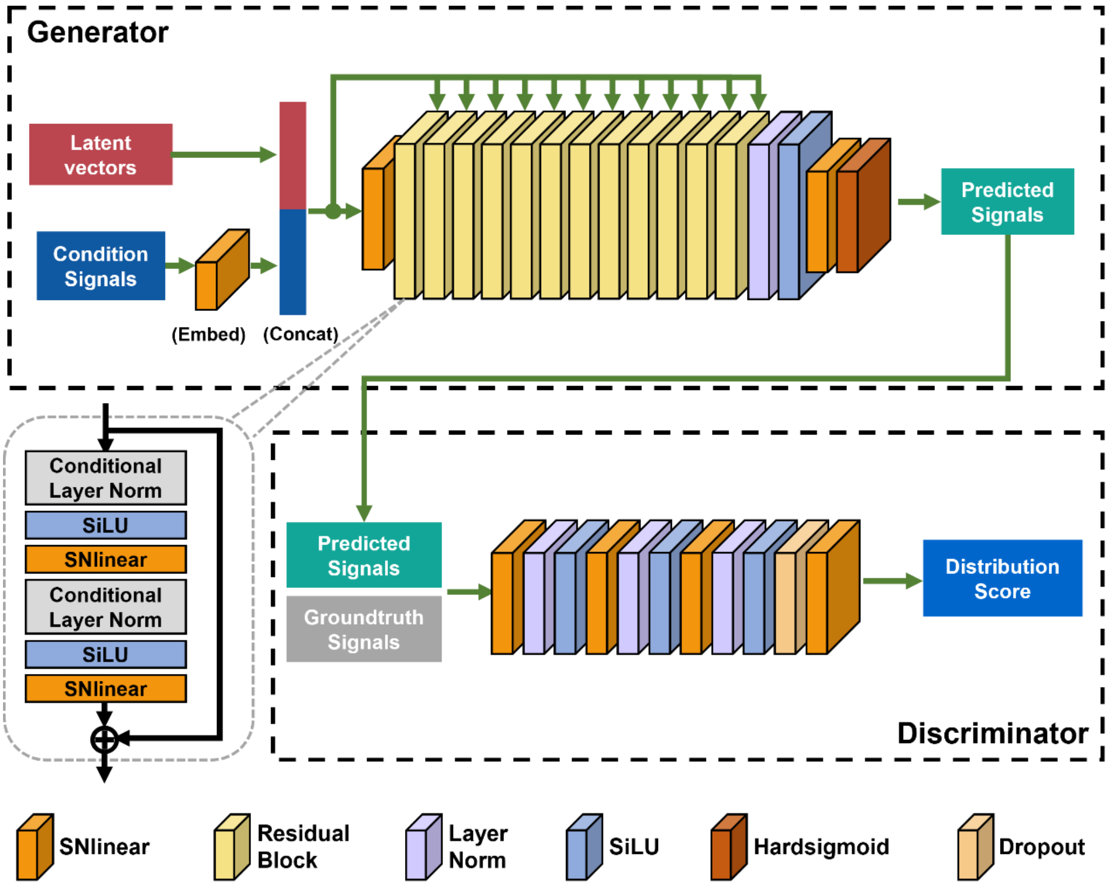

Figure S9. Diagram of c-GAN architecture for spectral reconstruction.

Generator Architecture	
Module	Configuration
Condition Embed	SNLinear(21,64)
Latent Fusion	SNLinear(128,512)
Residual Blocks	10×[Conditional Layer Norm→SiLU→SNLinear(512,512)]
Output Layer	LayerNorm→SiLU→SNLinear(512,261)→Hardsigmoid
Discriminator Architecture	
Module	Configuration
Feature Blocks	3×[SNLinear→LayerNorm→SiLU] (256 units)
Regularization	Dropout(90%)
Prediction Head	SNLinear(256,1)
Note: SNLinear, Spectral Normalization Linear.	

Table S1. Architecture setting of the c-GAN model

6. Simulation Evaluation

Fig. S10 presents representative single-peak spectral reconstructions under the 30 dB SNR conditions, demonstrating case-specific reconstruction performance.

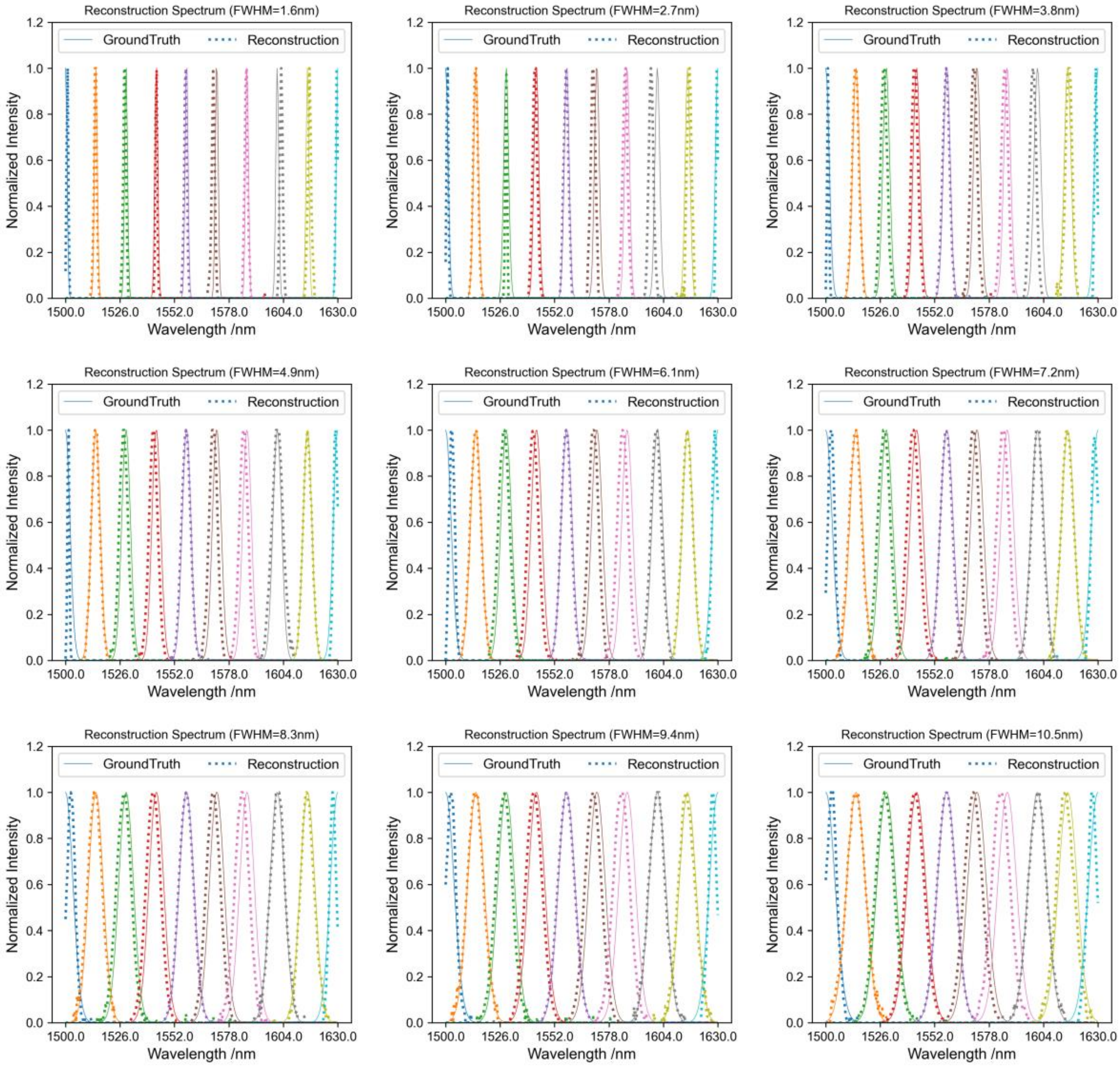

Figure S10. Single-peak spectral reconstructions at 30 dB SNR across 1.6–10.5 nm FWHM bandwidths.

7. Experimental Setup

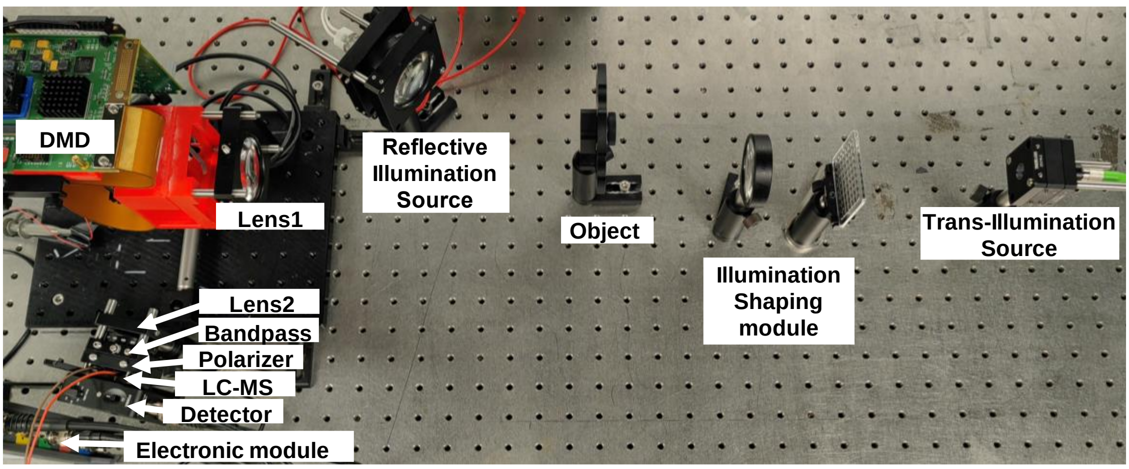

Figure S12. Experimental realisation of the hyperspectral single-pixel imaging system.

As shown in Fig. S1, the implemented system architecture (corresponding to Fig. 1a) consisted of a binary-patterned test target illuminated by reflective/transmissive broadband sources to generate hyperspectral scenes. Spectral calibration was conducted using a tunable laser (EXFO T100s-HP, 1500-1630 nm) as a narrow-linewidth illumination source, maintaining constant optical power with 1 pm spectral resolution across the operating band. For hyperspectral acquisition, an imaging lens (Lens1) projected target scenes onto a DMD spatial light modulator (VIALUX DLP V-650L; TI DLP650LNIR chip), which encoded spatial information via Hadamard basis patterns. The modulated optical signal traversed a quad-fold optical path before being focused into a single-point beam by Lens 2. This beam underwent spectral modulation by the electrically-controlled liquid crystal metasurface (LC-MS), subsequent detection by a single-pixel InGaAs photodetector (Thorlabs PDA20CS2), and signal digitisation via ADC electronics. The bandpass filter and polariser adjacent to the LC-MS rejected uncalibrated polarisation/wavelength components that would otherwise introduce significant measurement noise.

Reference

1. Sun, M.-J., Meng, L.-T., Edgar, M. P., Padgett, M. J. & Radwell, N. A Russian Dolls ordering of the Hadamard basis for compressive single-pixel imaging. *Sci Rep* **7**, 3464 (2017).
2. Frank, F. C. I. Liquid crystals. On the theory of liquid crystals. *Discuss. Faraday Soc.* **25**, 19 (1958).
3. Welford, K. R. & Sambles, J. R. Analysis of Electric Field Induced Deformations in a Nematic Liquid Crystal for any Applied Field. *Molecular Crystals and Liquid Crystals* **147**, 25–42 (1987).
4. Dai, P. *et al.* Inverse design of structural color: finding multiple solutions *via* conditional generative adversarial networks. *Nanophotonics* **11**, 3057–3069 (2022).
5. Fan, Y. *et al.* Dispersion-assisted high-dimensional photodetector. *Nature* (2024) doi:10.1038/s41586-024-07398-w.